Int J Fract (2016) 200:77–98
DOI 10.1007/s10704-016-0130-x

IUTAM PARIS 2015

Critical hardening rate model for predicting path-dependent ductile fracture

Stephane J. Marcadet · Dirk Mohr

Received: 6 January 2016 / Accepted: 14 June 2016 / Published online: 29 June 2016

Abstract A new phenomenological framework for predicting ductile fracture after non-proportional loading paths is proposed, implemented into FE software and validated experimentally for a limited set of monotonic and reverse loading conditions. Assuming that ductile fracture initiation is imminent with the formation of a shear band, a shear localization criterion in terms of the elastoplastic tangent matrix is sufficient from a theoretical point of view to predict ductile fracture after proportional and non-proportional loading. As a computationally efficient alternative to analyzing the acoustic tensor, a phenomenological criterion is proposed which expresses the equivalent hardening rate at the onset of fracture as a function of the stress triaxiality and the Lode angle parameter. The mathematical form of the criterion is chosen such that it reduces to the Hosford–Coulomb criterion for proportional loading. The proposed framework implies that the plasticity model is responsible for the effect of loading history on ductile fracture. Important non-isotropic hardening features such as the Bauschinger effect, transient softening and hardening stagnation must be taken into account by the plasticity model formulation to obtain reasonable fracture predictions after non-proportional loading histories. A new comprehensive plasticity model taking the above effects into account is thus an important byproduct of this work. In addition, compression–tension and reverse-shear experiments are performed on specimens extracted from dual-phase steel sheets to validate the proposed plasticity and fracture model.

Keywords Ductile fracture · Localization · Hardening rate · Reverse loading · Reverse shear · Hosford–Coulomb

S. J. Marcadet
Impact and Crashworthiness Laboratory, Department of Mechanical Engineering, Massachusetts Institute of Technology, Cambridge, MA, USA

D. Mohr (✉)
Department of Mechanical and Process Engineering, Swiss Federal Institute of Technology (ETH), Zurich, Switzerland
e-mail: dmohr@ethz.ch

1 Introduction

Since the pioneering work of Gurson (1977), porous plasticity models have received considerable attention because of their sound micromechanical basis and ability to predict fracture in many applications. Inspired by the early work of McClintock (1968) and Rice and Tracey (1969), Gurson-type of models have been developed to provide a mathematical description of the nucleation, growth and coalescence of voids in solids. It is undisputed that these mechanisms are relevant at high stress triaxialities such as encountered in front of crack tips (e.g. Needleman and Tvergaard 1987). In crack-free sheet materials, the stress state is usually close to plane stress and hence the void growth driving stress triaxiality is usually below the theoretical maxi-

mum value of 2/3. Even inside a localized neck where three-dimensional stress states develop, the stress triaxiality seldom exceeds values of 0.8. Consequently, there is limited void growth in a statistically homogeneous sense in sheet specimens prior to fracture initiation. This conclusion is partially supported by experimental observations of Ghahremaninezhad and Ravi-Chandar (2012, 2013) from micrographs taken at different stages during tension and shear experiments on aluminum alloy 6061-T6, and the synchrotron X-ray laminography observations of Morgeneyer et al. (2014) for aluminum alloy 2198.

At the macroscopic level, there is also growing evidence that the stress–strain response of sheet metal can be predicted with high accuracy up to the point of fracture initiation using non-porous plasticity models. The decrease in the force level that is observed in the post-necking range can usually be described without introducing damage into the material model. However, as shown by Dunand and Mohr (2010), Sung et al. (2010), Tardif and Kyriakides (2012) and Mohr and Marcadet (2015), a careful identification of the large strain hardening response of non-porous models through inverse procedures is required. Despite the physically sound formulation of Gurson models, it is very difficult to find experimental evidence that justifies their application to sheet metal as far as the description of the elasto-plastic material response is concerned. It is reemphasized that this statement is made with regard to the *plasticity of sheet metal* only.

An ad-hoc approach to predicting ductile fracture with porous plasticity models is to assume that fracture initiates when the computed porosity reaches a critical value. A more physical approach would be to assume that the porous plasticity model provides an accurate description of the effect of porosity on the material's load carrying capacity which implies that ductile fracture is predicted "naturally". In other words, the solution of a boundary value problem will feature zones of plastic localization (e.g. dilatational shear bands) that will eventually cause the loss of load carrying capacity of the structure at hand. The study of Besson et al. (2003) of slant fracture nicely illustrates this approach. Such simulation models can be supplemented with coalescence criteria (see review by Benzerga and Leblond 2010) to account for localization events at the mesoscale. Note that the latter may even occur before macroscopic localization (Tekoglu et al. 2015).

Recent experimental evidence regarding ductile fracture at low stress triaxialities (e.g. Barsoum and Faleskog 2007; Mohr and Henn 2007; Haltom et al. 2013; Mohr and Marcadet 2015) is not in good agreement with the trends predicted by conventional Gurson models. The qualitative differences are mostly due to the fact that conventional Gurson models do not predict shear localization at low stress triaxialities (at reasonable magnitudes of strain). So-called shear-modified Gurson models have thus been developed to capture the localization at low stress triaxialities. An example is the work by Nahshon and Hutchinson (2008) who added a shear term to the void volume evolution law of the GTN model (Tvergaard and Needleman 1984) and demonstrated the importance of this modification in their predictions of shear localization. Danas and Ponte Castañeda (2012) used nonlinear homogenization to come up with a porous plasticity model that accounts for void shape changes (that are characteristic for shear loading). Their analysis also shows the loss of ellipticity at low stress triaxialities.

When using porous plasticity (e.g. Gurson 1977; Gologanu et al. 1993; Benzerga and Besson 2001; Monchiet et al. 2008) the evolution law for the void volume fraction (and other possible microstructural state variables) is loading path sensitive and failure predictions with microstructurally-informed coalescence criteria (e.g. Thomason 1985; Pardoen and Hutchinson 2000; Benzerga 2002; Tekoglu et al. 2015) are then loading path dependent. However, given the limited benefits of Gurson type of models as far as predicting the elasto-plastic response of sheet metal is concerned, the combination of non-porous plasticity models with damage indicator models provides an attractive framework for predicting loading path dependent fracture initiation in industrial practice. Different from porous plasticity and coalescence models, damage indicator models often have no physical basis and are at most physics-inspired. The damage indicator is a dimensionless scalar variable that evolves as a function of the stress state and plastic deformation,

$$dD = \frac{d\bar{\varepsilon}_p}{\bar{\varepsilon}_f^{pr}[\eta, \bar{\theta}]}. \tag{1}$$

It is initially zero while fracture is assumed to occur when $D = 1$. The heart of these models is the weight-

ing function $\bar{\varepsilon}_f^{pr}[\eta, \bar{\theta}]$, which provides the strain to fracture for proportional loading as a function of the stress triaxiality η and the Lode angle parameter $\bar{\theta}$. Bao and Wierzbicki (2004) provide a comprehensive overview on different stress-state dependent damage indicator models including weighting functions based on the works of McClintock (1968), Rice and Tracey (1969), LeRoy et al. (1981), Cockcroft and Latham (1968), Oh et al. (1979), Brozzo et al. (1972) and Clift et al. (1990). More recent representatives of this class of models are the modified Mohr–Coulomb model by Bai and Wierzbicki (2010) and the micro-mechanically motivated Hosford–Coulomb model by Mohr and Marcadet (2015). Even though the latter has been derived from a localization criterion for proportional loading only, it gives satisfactory results for both proportional and non-proportional loading paths (Bai 2008; Papasidero et al. 2015; Marcadet and Mohr 2015). The main shortcoming of damage indicator models is the lack of physical arguments justifying their validity for non-proportional loading paths. Even though the variable D is often called *damage* and Eq. (1) is referred to as damage accumulation rule, it is emphasized that D has no direct physical meaning (unlike the damage variable used in continuum damage mechanics). Instead, it may be more appropriate to view the damage indicator framework as a heuristic mathematical model for predicting path dependent fracture initiation.

The main objective of the present paper is to provide a mechanism-inspired model for predicting ductile fracture initiation under proportional and non-proportional loading. An important byproduct of this work is an advanced plasticity model which accounts for direction-dependent Lankford ratios, the Bauschinger effect, work hardening stagnation and quasi-permanent softening. The proposed model is validated using experimental data for two advanced high strength steels for proportional monotonic experiments, compression–tension experiments and reverse shear experiments.

2 Plasticity model

In view of predicting the large deformation and fracture response for non-proportional loading paths, a finite strain plasticity model formulation is presented that accounts for (i) loading direction dependent Lankford ratios, (ii) the early yield after load reversal (Bauschinger effect), (iii) the high hardening rate in the elasto-plastic transition regime resulting from load reversal (transient hardening), (iv) permanent softening, and (v) work hardening stagnation. Barlat et al. (2011) proposed an anisotropic hardening model based on homogeneous yield functions to describe these effects. As discussed in the review papers by Chaboche (2008) and Eggertsen and Mattiasson (2010; 2011), combinations of linear and non-linear hardening rules can account for the Bauschinger effect, transient hardening and permanent softening, while further model enrichments are necessary to account for hardening stagnation (e.g. Yoshida and Uemori 2002). To account for all five effects (i)–(v), Marcadet and Mohr (2015) proposed combining the plasticity models of Mohr et al. (2010) with the non-linear hardening models of Chaboche (2008) and Yoshida and Uemori (2002) type of hardening stagnation.

In the sequel, the model by Marcadet and Mohr (2015) is reformulated to simplify the associated material model parameter identification procedure. In particular, the hardening laws are formulated such that that the model parameters describing the material's response to monotonic loading do not need to be readjusted when calibrating the parameters that account for reverse loading effects. The model ingredients are chosen in view of modeling Advanced High Strength Steels (AHSS). The particular choice of the yield function and flow rule would need to be revisited before applying the model to non-ferrous metals such as aluminum or HCP materials. Also, further extensions of the back stress evolution rules are expected to be in order to describe the material behavior for severely non-proportional loading path changes (e.g. tension along the rolling direction followed by tension along the transverse direction).

2.1 Yield function and flow rule

To define the pressure-independent yield surface, we introduce the tensor $\boldsymbol{\xi}$ as a measure of the difference between the deviatoric Cauchy stress and a deviatoric back stress tensor $\mathbf{X}$,

$$\boldsymbol{\xi} = dev(\boldsymbol{\sigma}) - \mathbf{X}. \tag{2}$$

For most advanced high strength steel sheets, the monotonic axial stress–strain response is isotropic in

the plane of the sheet (e.g. Mohr et al. 2010). Consequently, the von Mises equivalent stress definition is employed

$$\bar{\xi} = \sqrt{\frac{3}{2}\boldsymbol{\xi} : \boldsymbol{\xi}} = \sqrt{\frac{3}{2}}\left|\tilde{\boldsymbol{\xi}}\right| \tag{3}$$

to define the yield surface,

$$f = \bar{\xi} - k_{iso} = 0, \tag{4}$$

with k_{iso} denoting the isotropic deformation resistance. In (3), $\tilde{\boldsymbol{\xi}}$ denotes the stress vector with the components

$$\tilde{\boldsymbol{\xi}} = \{\xi_{11}, \xi_{22}, \xi_{33}, \sqrt{2}\xi_{12}, \sqrt{2}\xi_{13}, \sqrt{2}\xi_{23}\}^T. \tag{5}$$

In the case of mildly direction-dependent Lankford ratios, we follow the recommendations of Stoughton (2002), Cvitanic et al. (2008) and Mohr et al. (2010) and employ a non-associated flow rule with a Hill'48 flow potential function,

$$d\boldsymbol{\varepsilon}_p = d\lambda \frac{\mathbf{G} : \boldsymbol{\xi}}{\sqrt{\boldsymbol{\xi} : \mathbf{G} : \boldsymbol{\xi}}}, \tag{6}$$

with the plastic multiplier $d\lambda$ and the positive-definite fourth-order tensor **G.** When adopting vector notation for the stress arguments, **G** can be represented by the symmetric matrix

$$\tilde{\mathbf{G}} = \begin{bmatrix} 1 & G_{12} & -(1+G_{12}) & 0 & 0 & 0 \\ G_{12} & G_{22} & -(G_{22}+G_{12}) & 0 & 0 & 0 \\ -(1+G_{12}) & -(G_{22}+G_{12}) & 1+2G_{12}+G_{22} & 0 & 0 & 0 \\ 0 & 0 & 0 & G_{44}/2 & 0 & 0 \\ 0 & 0 & 0 & 0 & 1.5 & 0 \\ 0 & 0 & 0 & 0 & 0 & 1.5 \end{bmatrix}. \tag{7}$$

such that

$$\bar{\xi}^2_{Hill} = \boldsymbol{\xi} : \mathbf{G} : \boldsymbol{\xi} = \tilde{\boldsymbol{\xi}} \cdot \tilde{\mathbf{G}} \tilde{\boldsymbol{\xi}}. \tag{8}$$

The von Mises definition is adopted to define the equivalent plastic strain, i.e.

$$d\bar{\varepsilon}_p = \sqrt{\frac{2}{3} d\boldsymbol{\varepsilon}^p : d\boldsymbol{\varepsilon}^p}. \tag{9}$$

2.2 Hardening laws

The hardening laws are chosen based on the Combined Chaboche-Yoshida (CCY) model proposed by Marcadet and Mohr (2015). An attempt is made to simplify the model parameter identification by introducing a function B that describes the material hardening response for monotonic uniaxial tension along the rolling direction. For this special case, the yield condition reads

$$\sigma_{11} = k_{iso} + k_{kin} = B \tag{10}$$

with k_{iso} denoting the isotropic deformation resistance as introduced in Eq. (4), and k_{kin} denoting the back stress.

In most plasticity models, established analytical forms (Holomon, Swift, Voce, power law, exponential function, etc) are used to parametrize the isotropic hardening law

$$k_{iso} = k_{iso}[\bar{\varepsilon}_p]. \tag{11}$$

The special feature of the current model is that a parametric form is used to describe B as a function of the equivalent plastic strain. In particular, we approximate the monotonic stress–strain response through a combined Swift–Voce law,

$$B = wA\left(\varepsilon_0 + \bar{\varepsilon}^p\right)^n + (1-w)\left\{Y_0 + Q\left(1 - e^{-b_V \bar{\varepsilon}^p}\right)\right\}, \tag{12}$$

with the Swift parameters $\{A, \varepsilon_0, n\}$, the Voce parameters $\{Y_0, Q, b_V\}$, and the weighting factor $0 \leq w \leq 1$. Both the Swift and the Voce form can be well-fitted to the stress–strain curves measured up to the point of necking in uniaxial tension experiments. However, the Voce hardening law usually underestimates the strain hardening at large strains, while the opposite holds true for the Swift law. The combined Swift–Voce law features an additional weighting factor as parameter which can be conveniently identified through inverse analy-

sis of the specimen response in the post-necking range (e.g. Mohr and Marcadet 2015; Gu and Mohr 2015). The repartition of the effective hardening response into isotropic and kinematic hardening will then be described through additional constitutive equations.

For general 3D settings, k_{iso} and k_{kin} will serve as internal variables of the constitutive model. For notational convenience, we also introduce the sum of k_{iso} and k_{kin} as dependent variable,

$$k = k_{iso} + k_{kin}. \tag{13}$$

The initial configuration of the material is then characterized through the initial condition

$$\begin{aligned} @\bar{\varepsilon}_p = 0: \quad & k = k_{iso} \\ & = B_0 := wA\varepsilon_0^n + (1-w)\,Y_0 \text{ and } k_{kin} = 0. \end{aligned} \tag{14}$$

For arbitrary three-dimensional loading, the stress B defines a bounding limit for k,

$$k \leq B, \tag{15}$$

while the evolution of k is expressed through the differential equation

$$dk = S\left\{dB + \gamma_\beta\,(B-k)\,d\bar{\varepsilon}_p\right\} \tag{16}$$

where $S \in [0, 1]$ is an additional internal variable associated with hardening stagnation. For loading paths without any hardening stagnation (e.g. monotonic uniaxial tension), we have $S = 1$ at all times, and consequently $dk = dB$ and $k = B$. In the case where work hardening stagnation occurs, the strict inequality $k < B$ holds true. The recovery term $\gamma_\beta\,(B-k)\,d\bar{\varepsilon}_p$ allows the variable k to converge towards B whenever the material deformed outside the hardening stagnation regime ($S = 1$).

There is experimental evidence that the hardening of rolled steel sheets after loading reversals must be mostly kinematic to accurately describe the Bauschinger effect (Yoshida and Uemori 2002). However, when introducing complex evolution laws in the constitutive equations, special attention is required with regards to thermodynamic constraints. For these reasons, the repartition between isotropic and kinematic hardening is prescribed through the equation

$$dk_{iso} = \begin{cases} 0 & \text{if } k_{kin} < \varphi k_{iso} \\ \frac{dk}{1+\varphi} & \text{if } k_{kin} = \varphi k_{iso} \end{cases} \tag{17}$$

with the model parameter $\varphi \geq 0$; this particular form of the evolution law ensures that $k_{kin} \leq \varphi k_{iso}$ is always fulfilled. According to (17), the apparent strain hardening under uniaxial tension (evolution of B) is entirely due to kinematic hardening, until $B = (1+\varphi)B_0$.

2.3 Evolution of the back stress tensor

2.3.1 General form of the back stress evolution equations

The evolution rules for the back stress tensors will be a combination of terms inspired by the classic Prager (1956) and Armstrong and Frederick (1966) formulations:

$$d\mathbf{x} = \frac{2}{3}H d\boldsymbol{\varepsilon}_p + \gamma\left(\frac{2}{3}k d\boldsymbol{\varepsilon}_p - \mathbf{x}d\lambda\right). \tag{18}$$

The first term of the right hand side of (18) represents linear kinematic hardening. Under proportional loading, it is macroscopically equivalent to isotropic hardening with a tangent modulus H. The second term of the right hand side is motivated by the dynamic recovery in the Armstrong and Frederick (1966) formulation. After loading reversal, the back stress tensor is expected to remain within a sphere of radius k in the deviatoric stress space. The particular feature of our evolution laws is that the radius of the bounding sphere may evolve. This feature mimics the behavior of two surface models (e.g. Dafalias and Popov 1976). For monotonic loading, the back stress evolution is only due to the first right hand side term. After loading reversal, the back stress contribution of the first term is negligibly small as compared to the second term during the transition phase until the backstress approaches the sphere boundary.

2.3.2 Evolution law for permanent softening

In order to account for permanent softening and hardening stagnation, we make use of two back stress tensors,

$$\mathbf{X} = \boldsymbol{\alpha} + \boldsymbol{\beta}. \tag{19}$$

The evolution rule for the back stress tensor $\boldsymbol{\beta}$ accounts for permanent softening (Fig. 1a) and kinematic hardening at large strains (Fig. 1b); it is defined through the differential equation

$$d\boldsymbol{\beta} = \frac{2}{3}\left(\frac{dk_\beta}{d\bar{\varepsilon}_p}\right) d\boldsymbol{\varepsilon}_p + S\gamma_\beta \left(\frac{2}{3} k_\beta d\boldsymbol{\varepsilon}_p - \boldsymbol{\beta} d\lambda\right). \quad (20)$$

As mentioned above, the proposed evolution rule is a combination of terms inspired by the classic Prager (1956) and Armstrong and Frederick (1966) formulations. However, different from Prager's linear kinematic hardening rule which makes use of a constant modulus, the hardening modulus $dk_\beta/d\bar{\varepsilon}_p$ of the Prager term (first term of the right hand side) is bounded by the evolution of the variable k_{kin}. Formally, this nonlinearity is introduced through the constraint

$$\frac{dk_\beta}{d\bar{\varepsilon}_p} = \min\left(C_\beta, \frac{dk_{kin}}{d\lambda}\right) \quad (21)$$

which typically becomes active at large strains and for large values of C_β. Similarly, different from Armstrong–Frederick's kinematic hardening rule which makes use of a constant radius, the radius of the bounding surface for the back stress evolution is controlled by the variable k_β. Note that the Armstrong–Frederick recovery effect on the back stress evolution (second term on the right hand side of Eq. 20) is interrupted during work hardening stagnation.

2.3.3 Evolution law for Bauschinger effect

Analogously to the evolution equations of the back stress $\boldsymbol{\beta}$, we define the hardening law for $\boldsymbol{\alpha}$ to represent the Bauschinger effect and transient hardening (Fig. 1c),

$$d\boldsymbol{\alpha} = \frac{2}{3}\left(\frac{dk_\alpha}{d\bar{\varepsilon}_p}\right) d\boldsymbol{\varepsilon}^p + \gamma_\alpha \left(\frac{2}{3} k_\alpha d\boldsymbol{\varepsilon}^p - \alpha d\lambda\right) \quad (22)$$

with the model parameter γ_α and the coupling constraint

$$dk_\alpha = dk_{kin} - dk_\beta. \quad (23)$$

As discussed in Marcadet and Mohr (2015), the evolution of $\boldsymbol{\alpha}$ is not affected by hardening stagnation.

2.4 Work hardening stagnation

As for the CCY model (Marcadet and Mohr 2015), the constitutive equations for the evolution rule of S are inspired by the work of Yoshida and Uemori (2002). Work hardening stagnation (Fig. 1d) is activated as a function of the loading history. Firstly, the strain-like measure $\boldsymbol{\omega}$ is introduced to characterize the loading path,

$$d\boldsymbol{\omega} = \frac{2}{3} \frac{\boldsymbol{\xi}}{\sqrt{\frac{3}{2}\boldsymbol{\xi} : \boldsymbol{\xi}}} d\lambda. \quad (24)$$

The distance of $\bar{\omega}$ to a point $\mathbf{q}$ is then defined as

$$\bar{\omega} = \sqrt{\frac{2}{3}(\boldsymbol{\omega} - \mathbf{q}) : (\boldsymbol{\omega} - \mathbf{q})}. \quad (25)$$

and limited to

$$\bar{\omega} - r \leq 0. \quad (26)$$

When $\bar{\omega} = r$ and $(\boldsymbol{\omega} - \mathbf{q}) : d\boldsymbol{\omega} > 0$, r and $\mathbf{q}$ are updated according to

$$d\mathbf{q} = (1 - h) \cdot d\boldsymbol{\omega} \quad (27)$$

$$dr = h \frac{(\boldsymbol{\omega} - \mathbf{q})}{\bar{\omega}} : d\boldsymbol{\omega}. \quad (28)$$

The internal variable S is then defined as

$$S[\boldsymbol{\omega}, \mathbf{q}, r] = \begin{cases} \text{if } (\boldsymbol{\omega} - \mathbf{q}) : d\boldsymbol{\omega} \geq 0 \text{ then } \frac{\bar{\omega}}{r} \\ \text{if } (\boldsymbol{\omega} - \mathbf{q}) : d\boldsymbol{\omega} < 0 \text{ then } 0 \end{cases} \quad (29)$$

The variable S corresponds to the ratio of the distance of $\boldsymbol{\omega}$ to $\mathbf{q}$ when $\bar{\omega}$ increases. It is set to zero when it decreases. This means that the hardening is deactivated in case of reverse loading and progressively reactivated at large strains after reversal.

2.5 Thermodynamic constraints

The starting point of our considerations is the free energy imbalance (e.g. Gurtin et al. 2013) of the form

$$\dot{\psi} \leq \boldsymbol{\sigma} : \dot{\boldsymbol{\varepsilon}} \quad (30)$$

The free energy is limited to an elastic part ψ_e

$$\psi = \psi_e, \quad (31)$$

which must be positive, i.e.

$$\psi_e \geq 0. \quad (32)$$

Assuming the quadratic elastic strain energy potential:

$$\psi_e = \frac{1}{2}\left(\mathbf{C} : (\boldsymbol{\varepsilon} - \boldsymbol{\varepsilon}_p)\right) : (\boldsymbol{\varepsilon} - \boldsymbol{\varepsilon}_p) \quad (33)$$

along with the elastic constitutive equation:

$$\boldsymbol{\sigma} = \frac{\partial \psi}{\partial(\boldsymbol{\varepsilon} - \boldsymbol{\varepsilon}_p)} = \mathbf{C} : (\boldsymbol{\varepsilon} - \boldsymbol{\varepsilon}_p) \quad (34)$$

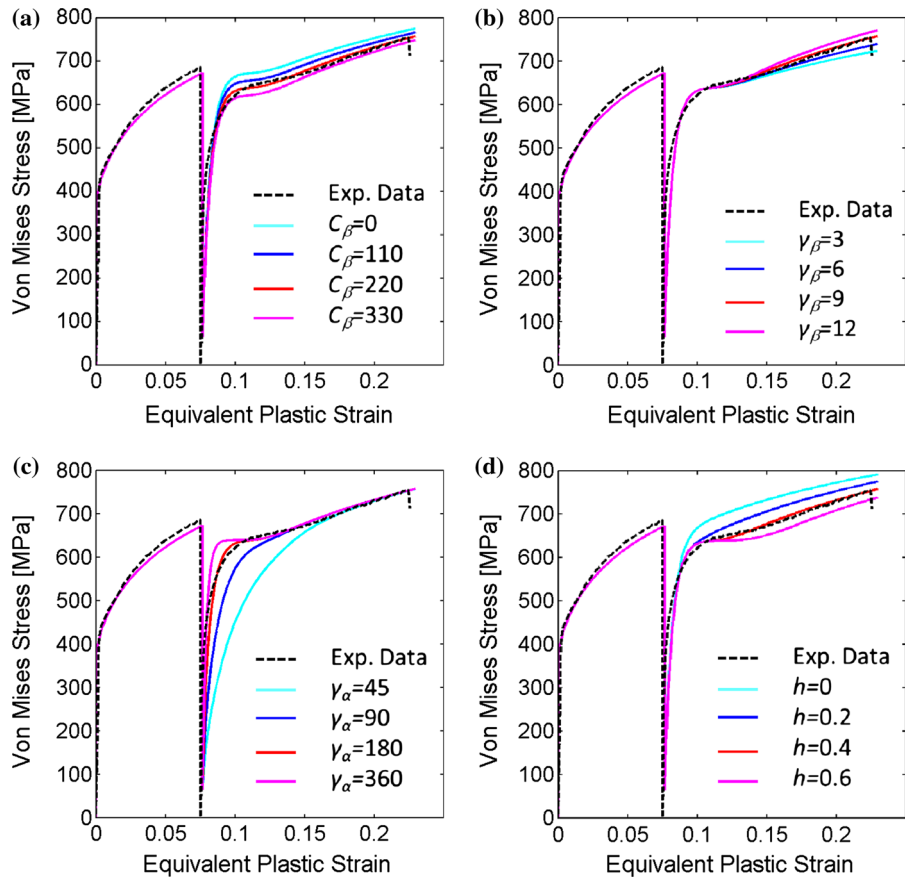

Fig. 1 Illustration of the effects of selected kinematic hardening model parameters for a DP600 steel: **a** permanent softening parameter C_β, **b** parameter γ_β, **c** Bauschinger parameter γ_α, **d** stagnation parameter h. The default parameters are $\gamma_\alpha = 180$, $C_b = 220\,\text{MPa}$, $h = 0.4$ and $\gamma_b = 9$

the free energy imbalance may be substituted by the requirement of nonnegative rate of plastic dissipation,

$$\dot{d}_p = \boldsymbol{\sigma} : \dot{\boldsymbol{\varepsilon}}_p \geq 0. \tag{35}$$

Combining Eqs. (2), (6), (19) and (35), we obtain the rate of plastic dissipation

$$\dot{d}_p = (\boldsymbol{\alpha} + \boldsymbol{\beta} + \boldsymbol{\xi}) : \dot{\boldsymbol{\varepsilon}}_p = \underbrace{\bar{\xi}_{Hill}\dot{\lambda}}_{\geq 0} + \frac{(\boldsymbol{\alpha} + \boldsymbol{\beta}) : \mathbf{G} : \boldsymbol{\xi}}{\bar{\xi}_{Hill}}\dot{\lambda}. \tag{36}$$

The first term is unconditionally nonnegative. However, $(\boldsymbol{\alpha} + \boldsymbol{\beta}) : \mathbf{G} : \boldsymbol{\xi}$ may become negative. The non-zero dissipation condition requires that

$$-(\boldsymbol{\alpha} + \boldsymbol{\beta}) : \mathbf{G} : \boldsymbol{\xi} \leq \bar{\xi}^2_{Hill}. \tag{37}$$

The left hand side of (36) is bound by

$$\begin{aligned} -(\boldsymbol{\alpha} + \boldsymbol{\beta}) : \mathbf{G} : \boldsymbol{\xi} &\leq |(\boldsymbol{\alpha} + \boldsymbol{\beta}) : \mathbf{G} : \boldsymbol{\xi}| \\ &= \left|\tilde{\mathbf{G}}\left(\tilde{\boldsymbol{\alpha}} + \tilde{\boldsymbol{\beta}}\right) \cdot \tilde{\boldsymbol{\xi}}\right| \\ &\leq \left|\tilde{\mathbf{G}}\left(\tilde{\boldsymbol{\alpha}} + \tilde{\boldsymbol{\beta}}\right)\right| \left|\tilde{\boldsymbol{\xi}}\right| \leq \lambda_{\max} \left|\tilde{\boldsymbol{\alpha}} + \tilde{\boldsymbol{\beta}}\right| \left|\tilde{\boldsymbol{\xi}}\right| \end{aligned} \tag{38}$$

while a lower bound for the right hand side term in (36) reads

$$\bar{\xi}^2_{Hill} = \tilde{\boldsymbol{G}}\tilde{\boldsymbol{\xi}} \cdot \tilde{\boldsymbol{\xi}} \geq \lambda_{\min} \left|\tilde{\boldsymbol{\xi}}\right|^2 \tag{39}$$

with $\lambda_{\max}$ and $\lambda_{\min}$ denoting the largest and smallest positive eigenvalues of the symmetric $\tilde{\mathbf{G}}$ matrix. Combining the above inequalities leads to the constraint

$$\lambda_{\max} \left|\tilde{\boldsymbol{\alpha}} + \tilde{\boldsymbol{\beta}}\right| \leq \lambda_{\min} \left|\tilde{\boldsymbol{\xi}}\right| \tag{40}$$

Inserting the bounds provided by the kinematic and isotropic hardening laws, we obtain

$$\lambda_{\max} \frac{2}{3} k_{kin} \leq \lambda_{\min} \sqrt{\frac{2}{3}} k_{iso} \tag{41}$$

This constraint means that the sum of the back stresses is bounded by the current isotropic yield surface. It is readily fulfilled if the model parameter φ [see Eq. (17)] is chosen such that

$$\varphi \leq \frac{\lambda_{\min}}{\lambda_{\max}} \sqrt{\frac{3}{2}}. \tag{42}$$

3 Critical hardening rate fracture initiation model

We are concerned with predicting the instant of ductile fracture initiation in structural applications such as sheet metal forming or the crush loading of thin-walled structures. The applicability of our model will be limited to materials and structural applications where a shear band forms prior to the formation of a crack. Furthermore, it will be assumed that the deformation accumulated within a shear band prior to fracture is not relevant for assessing the structural performance. In other words, there is no need to model the post shear-localization response. At the length and time scales of interest, it shall be reasonable to assume that the formation of a crack is imminent with the formation of a shear localization band. We emphasize that the physics of shear localization and fracture are fundamentally different. However, with the above working assumptions in place, we will no longer carefully differentiate between shear localization and fracture. It will actually be postulated that shear localization is the governing mechanism leading to ductile fracture, which is the basis for to the development of a "mechanism-inspired" ductile fracture initiation model.

The results from a notched tension experiment on a TRIP780 steel (Fig. 2) illustrate the above working assumption. After accumulating an equivalent plastic strain of 0.18 up to the force maximum (Fig. 2a), a through-thickness neck develops at the specimen center. Within this neck, the deformation increases further up to strains of 0.47, before a slant shear band forms (blue solid triangle) and the specimen fractures (black solid triangle). At the structural level, the displacement up to the force maximum is 1.55 mm, another 0.55 mm displacement increment is accumulated during necking until fracture initiates at $u_f = 2.10$ mm; the displacement increment between the instant of shear localization and fracture is almost zero at the scale of the macroscopic displacement recordings. It was only in a specimen from an experiment interrupted at a displacement of $0.99u_f$ (blue solid triangle in Fig. 2a), where we could detect some evidence of an emerging shear band of a width a few microns (order of grain size).

Even though the modeling assumption is expected to hold true for many engineering materials, it is noted

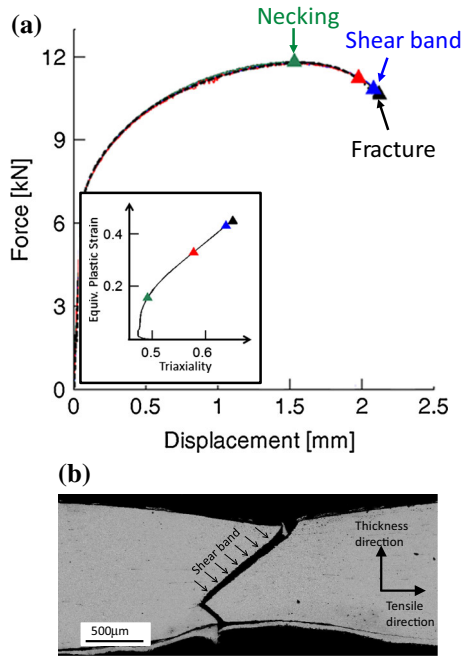

Fig. 2 **a** Force-displacement response of a flat notched tension specimen extracted from a 1.4 mm thick TRIP780 steel sheet, the insert shows the evolution of the equivalent plastic strain at the specimen center as a function of the stress triaxiality, **b** micrograph of a longitudinal cut through the fractured NT20 specimen

that it does not apply to materials such as superplastic metals or metallic glasses. For example, the formation of intense localized shear bands is the main deformation mechanism in metallic glasses for accommodating substantial inelastic strains at low homologous temperatures without fracturing (e.g. Anand and Su 2005). For the sake of simplicity, we will also limit our attention to the formulation of an isotropic fracture initiation model. The developments below would need to be repeated on the basis of the anisotropic Hosford–Coulomb model (Gu and Mohr 2015) in the case of materials that exhibit a pronounced anisotropic fracture response. Note that the complexity of the plasticity model (Sect. 2) remains almost unchanged when extending the model from isotropic to anisotropic plastic flow. Consequently, the mild anisotropy in the Lankford ratios is taken into account. As far as the fracture modeling is concerned, the model complexity increases significantly from the isotropic to the anisotropic formulation. Consequently, we recommend neglecting the effect of anisotropy on the fracture initiation except

in the case of severely anisotropic materials (e.g. aluminum extrusions).

3.1 Mechanism-based modeling

Assuming that the initiation of ductile fracture, i.e. the formation of macroscopic cracks in metals is imminent with the onset of localization, the onset of ductile fracture can be predicted through an infinite band-type of localization analysis (Rice 1976). For a material obeying the incremental stress–strain relationship

$$d\boldsymbol{\sigma} = \mathbf{L} : d\boldsymbol{\varepsilon}, \tag{43}$$

Rice (1976) showed that the condition for localization in a planar band reads

$$\det[L_{ijkl} n_k n_l] = 0 \tag{44}$$

with $\mathbf{n}$ denoting the unit normal vector to the localization band. Rice (1976) has also shown that the above bifurcation condition describes the loss of ellipticity of the governing field equation. It is worth noting that Rice's criterion remains valid irrespective of the loading history. The loading history effect on the onset of shear localization is solely described by the plasticity model which provides the evolution of the elasto-plastic tangent matrix $\mathbf{L}$ (fourth-order tensor) and the stress tensor $\boldsymbol{\sigma}$ (which enters into the corresponding finite strain formulation, see Mear and Hutchinson 1985). In engineering practice, the above approach is seldom used due to the high computational costs associated with solving equation (44) and its incompatibility with non-porous plasticity models (when predicting localization at low stress triaxialities).

3.2 Phenomenological modeling for proportional loading

As an alternative to bifurcation analysis, engineers often use fracture initiation criteria that provide the equivalent plastic strain to fracture as a function of the stress state,

$$\bar{\varepsilon}_f^{pr} = \bar{\varepsilon}_f^{pr}[\eta, \bar{\theta}]. \tag{45}$$

The existence of a fracture envelope can be justified for proportional loading in stress space. Mohr and Marcadet (2015) have shown that any envelope in stress space can be transformed into the form of (45) for materials featuring isotropic hardening only. For example, the Hosford–Coulomb model in *principal stress space* $\{\sigma_I, \sigma_{II}, \sigma_{III}\}$ reads

$$\bar{\sigma}_{HF} + c(\sigma_I + \sigma_{III}) = b \tag{46}$$

with the isotropic (Hosford 1972) scalar measure of the deviatoric stress tensor,

$$\bar{\sigma}_{HF} = \left\{ \frac{1}{2} \left((\sigma_I - \sigma_{II})^a + (\sigma_{II} - \sigma_{III})^a + (\sigma_I - \sigma_{III})^a \right) \right\}^{\frac{1}{a}} \tag{47}$$

and the model parameters $\{a, b, c\}$. Using coordinate transformations, the same criterion may be expressed in terms of the stress triaxiality, Lode parameter and Mises equivalent stress. In the *modified Haigh–Westergaard space* $\{\eta, \bar{\theta}, \bar{\sigma}\}$, we have,

$$\bar{\sigma} = \bar{\sigma}_f[\eta, \bar{\theta}] = \frac{b}{\left\{ \frac{1}{2} \left((f_1 - f_2)^a + (f_2 - f_3)^a + (f_1 - f_3)^a \right) \right\}^{\frac{1}{a}} + c(2\eta + f_1 + f_3)}. \tag{48}$$

with the Lode angle parameter dependent functions

$$\begin{aligned} f_1[\bar{\theta}] &= \frac{2}{3} \cos\left[\frac{\pi}{6} (1 - \bar{\theta}) \right], \\ f_2[\bar{\theta}] &= \frac{2}{3} \cos\left[\frac{\pi}{6} (3 + \bar{\theta}) \right], \\ f_3[\bar{\theta}] &= -\frac{2}{3} \cos\left[\frac{\pi}{6} (1 + \bar{\theta}) \right] \end{aligned} \tag{49}$$

For a Levy–von Mises material with isotropic hardening, a third representation of the Hosford–Coulomb criterion in the *mixed stress–strain space* $\{\eta, \bar{\theta}, \bar{\varepsilon}_p\}$ is readily obtained when using the inverse isotropic hardening law, $\bar{\varepsilon}_p = k^{-1}[\bar{\sigma}]$, to substitute the von Mises equivalent stress by the equivalent plastic strain,

$$\bar{\varepsilon}_f^{pr} = k^{-1} \left[\bar{\sigma}_f[\eta, \bar{\theta}] \right]. \tag{50}$$

In the latest coordinate frame transformation, we made use of the bijectivity of the isotropic hardening law $\bar{\sigma} = k[\bar{\varepsilon}_p]$.

The bijectivity of the hardening law allows us not only to substitute the equivalent von Mises stress through the equivalent plastic strain, but we can even express the fracture criterion in terms of a critical hardening rate, A fourth representation of the Hosford–Coulomb model can be given in the *mixed hardening rate & stress state space* $\{\eta, \bar{\theta}, d\bar{\sigma}/d\bar{\varepsilon}_p\}$,

$$\left(\frac{d\bar{\sigma}}{d\bar{\varepsilon}_p}\right)_f^{pr} = \frac{dk}{d\bar{\varepsilon}_p}\left[k^{-1}\left[\bar{\sigma}_f[\eta,\bar{\theta}]\right]\right]. \tag{51}$$

All four representations of the Hosford–Coulomb criterion have been visualized for plane stress conditions in Fig. 3 for a power law material

$$k[\bar{\varepsilon}_p] = A(\varepsilon_0 + \bar{\varepsilon}_p)^n. \tag{52}$$

with the Swift parameters $A = 1100\,\text{MPa}$, $\varepsilon_0 = 0.02$ and $n = 0.2$, and the Hosford–Coulomb parameters $a = 1.5$, $b = 1000\,\text{MPa}$ and $c = 0.1$. It is reemphasized that all four representations are fully equivalent and predict the same instant of fracture initiation for a given proportional loading path in stress space (under plane stress conditions).

3.3 Phenomenological modeling for non-proportional loading

As discussed in the introduction, we seek for a mechanism-based alternative to the heuristic damage indicator modeling framework to predict ductile fracture initiation for proportional *and non-proportional* loading paths. Aside from the lack of physical arguments supporting the particular mathematical form of the damage indicator framework, we also found a strong counterexample: experiments suggest an increase in the total strain to fracture after shear reversal (see Sect. 4.3.2). This is in contradiction with the prediction of damage indicator models which are insensitive to the effect of loading direction reversal for pure shear.

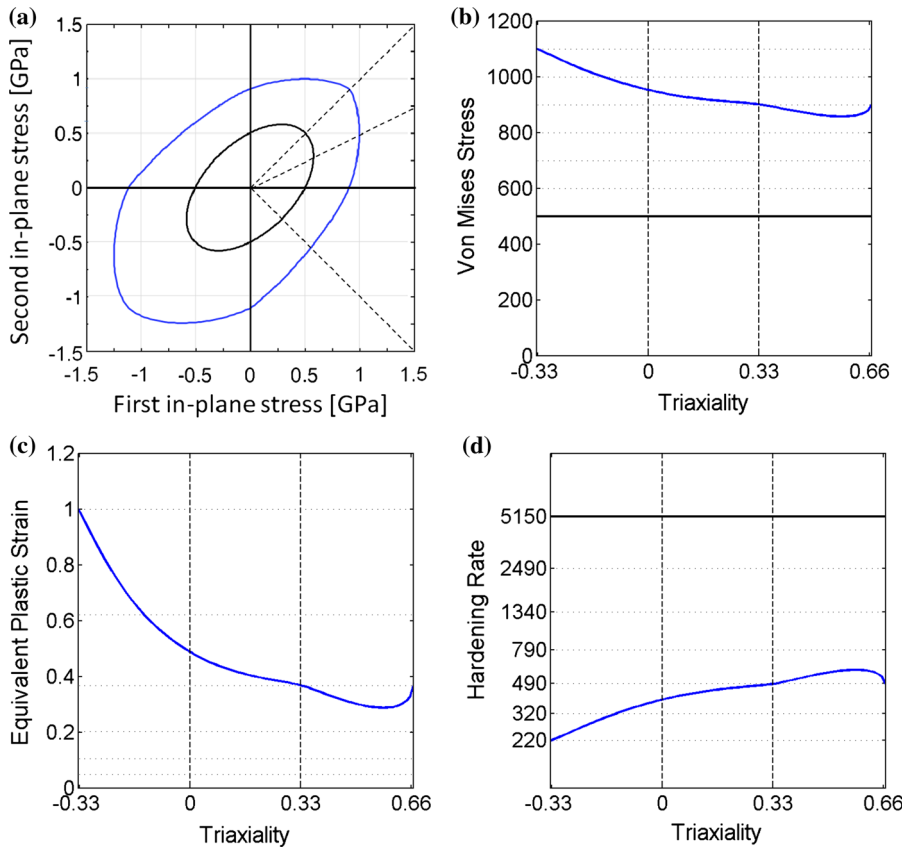

Fig. 3 Representation of the Hosford–Coulomb criterion for a power law material with plane stress condition in the following spaces **a** first and second in-plane stress components **b** modified Haigh–Westergaard space **c** mixed strain-stress state space **d** mixed hardening rate-stress state space. The initial Von Mises yield envelope (*solid black line*) and Hosford–Coulomb fracture locus (*solid blue line*) are shown

Inspired by the fact that Rice's (1976) localization criterion in terms of the tangent modulus $\mathbf{L}$ naturally incorporates the effect of the loading history, we propose a phenomenological derivative of Rice's model by postulating that ductile fracture initiates when the hardening rate $d\bar{\sigma}/d\bar{\varepsilon}$ reaches a critical value for a given stress state $\{\eta, \bar{\theta}\}$.

$$\left(\frac{d\bar{\sigma}}{d\bar{\varepsilon}}\right)_f = g[\eta, \bar{\theta}]. \tag{53}$$

Note that different from (51), we omit the superscript 'pr', i.e. criterion (53) is proposed to predict ductile fracture for both proportional and non-proportional loading paths. We also note that $d\bar{\varepsilon}$ defines the von Mises equivalent strain increment of the total strain tensor,

$$d\bar{\varepsilon} = \sqrt{\frac{2}{3} d\varepsilon : d\varepsilon}. \tag{54}$$

Similarly to Rice's localization criterion, the dependence on loading history of ductile fracture initiation is inherited from the plasticity model.

For materials exhibiting isotropic hardening only, the proposed model would reduce to a simple stress based criterion. This simple form for modeling the effect of loading history has been advocated by Stoughton and Yoon (2011). However, for materials exhibiting non-linear kinematic hardening (such as Bauschinger effect or permanent softening), the above model will immediately predict a history effect on ductile fracture.

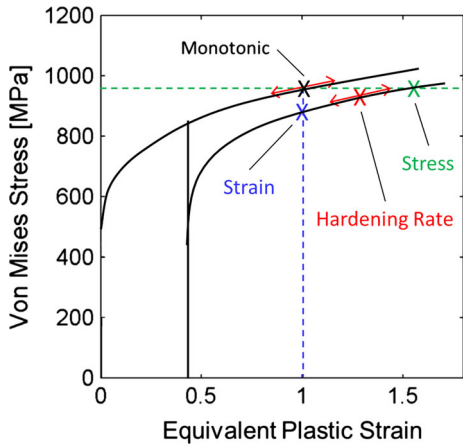

Fig. 4 Effect of plasticity on the prediction of fracture under reverse loading for the Hosford–Coulomb model as a function of the choice of critical quantity at fracture

This plasticity model effect is shown schematically in Fig. 4 and will be elaborated further in the subsequent sections dealing with real materials. The stress–strain relation is shown for monotonic and reverse loading after an equivalent plastic strain of 0.45. A constant stress state is assumed even after loading reversal (e.g. shear reversal). Fracture under monotonic loading is assumed to initiate at an equivalent plastic strain of 1. Figure 4 illustrates the effect of plasticity on the strain to fracture depending on the choice of critical quantity at fracture:

- von Mises stress, corresponding to Eq. (48), in green,
- equivalent plastic strain, corresponding to Eq. (50), in blue, and
- hardening rate, corresponding to Eq. (53), in red.

Note that all three models would yield the same strain to fracture when using an isotropic hardening model, while significant differences are observed for the model with kinematic hardening.

As far as the parametric form of $g[\eta, \bar{\theta}]$ is concerned, we suggest using (51) as evaluated for a power law hardening model with $n = 0.1$,

$$g[\eta, \bar{\theta}] = H_{UT} \left\langle \frac{\left\{\frac{1}{2}\left((f_1 - f_2)^a + (f_2 - f_3)^a + (f_1 - f_3)^a\right)\right\}^{\frac{1}{a}} + c(2\eta + f_1 + f_3)}{1 + c} \right\rangle^{\frac{1}{n}-1} \tag{55}$$

The proposed critical hardening rate model therefore features three model parameters: the critical hardening modulus H_{UT} for uniaxial tension, the friction coefficient c, and the Hosford exponent a. It is emphasized that (55) is merely a fitting function which has been chosen such that the critical hardening model inherits the capabilities of the Hosford–Coulomb model for proportional loading. A rigorous derivation of $g[\eta, \bar{\theta}]$ from the localization problem posed by (44) is a major undertaking which is deferred to future research.

3.4 Extended formulation

An important underlying assumption in the proposed ductile fracture model is that the fracture initiation is imminent with the onset of localization. There are a few exceptions where this assumption does not hold true. Consider for example a material in which Lüders' bands form (e.g. Hall 1970). In that case, localization bands occur temporarily, but cease rapidly as the hardening rate picks up. For such a material, the hardening rate right after initial yield is close to zero or even negative; the proposed model would predict fracture at this stage of loading even though significantly higher strains are attained in reality. A similar situation is encountered when PLC bands form in aluminum alloys (e.g. Benallal et al. 2006) or during work hardening stagnation after loading reversal in DP steels.

The common feature of these special cases is that the localization is stabilized rapidly due to the material's remaining hardening potential. Localization corresponds to a catastrophic event (i.e. fracture initiation), if there is no more hardening stabilization possible under continued monotonic loading along the current loading path. The failure criterion therefore must state that fracture occurs at an instant t_f if the localization criterion (53) is satisfied, and provided that the hardening modulus would not increase if the loading continued along the same strain path. Denoting the hardening modulus H at an instant t_f after loading along a specific strain path $\varepsilon[t]$ from the initial configuration ($t = 0$) to the current configuration ($t = t_f$) as

$$H\left[\boldsymbol{\varepsilon}[t_f]\right] := \left.\frac{d\bar{\sigma}}{d\bar{\varepsilon}}\right|_{t_f} \tag{56}$$

the fracture criterion is formally rewritten as

$$\max_{t \geq t_f} H\left[\boldsymbol{\varepsilon}[t_f] + \dot{\boldsymbol{\varepsilon}}[t_f](t - t_f)\right] \leq g\left[\eta[t_f], \bar{\theta}[t_f]\right]. \tag{57}$$

It is noted that the loading path assumed in (57) is only one possible post-localization scenario. As for propagating instabilities (e.g. Kyriakides 2001), the formation of a crack after the onset of localization also depends on the kinematic restrictions imposed by the surrounding material. In other words, different from the onset of localization, fracture initiation is expected to depend on the non-local conditions. It is also noted that the above model is not suitable for predicting fracture in the hardening stagnation regime after loading reversal.

3.5 Comment on the model sensitivity

At first sight, the formulation of a fracture initiation model in terms of the hardening rate appears to be more sensitive to experimental inaccuracies than models that are directly formulated in terms of strains. It is therefore worth emphasizing that the conversion from strains to hardening rates is only done computationally, i.e. the identification of the model parameters $\{a, H_{UT}, c\}$ is based on the measured strains to fracture for different stress states. Possible experimental uncertainties in the measurement of stress–strain curve slopes therefore do not enter the model parameter identification process.

The same applies to inaccuracies in the calibrated plasticity model. Even if the plasticity model provides only a poor approximation of the material's large deformation response, these plasticity model inaccuracies will not affect the model predictions of the strain to fracture for proportional loading. However, the model predictions for non-proportional loading depend on the slope accuracy of the plasticity model. In other words, in order to benefit from the model's ability to estimate of the strains to fracture after complex loading histories, it is necessary to use an adequate plasticity model. For instance, the increase in ductility after reverse shear loading is only possible if a plasticity model with nonlinear kinematic hardening or hardening stagnation is employed.

4 Experiments

4.1 Materials

The proposed plasticity and fracture models are validated based on the experimental data for two different materials: 1.0 mm thick DP780 steel sheets provided by US Steel, and 1.4 mm thick DP590 steel sheets provided by ArcelorMittal.

4.2 Specimens

In an attempt to obtain a comprehensive characterization of the plastic and fracture response of advanced high strength steels, the following types of experiments have been performed:

(a) Monotonic uniaxial tension (UT): tensile specimens with a 10 mm wide gage section (Fig. 5)

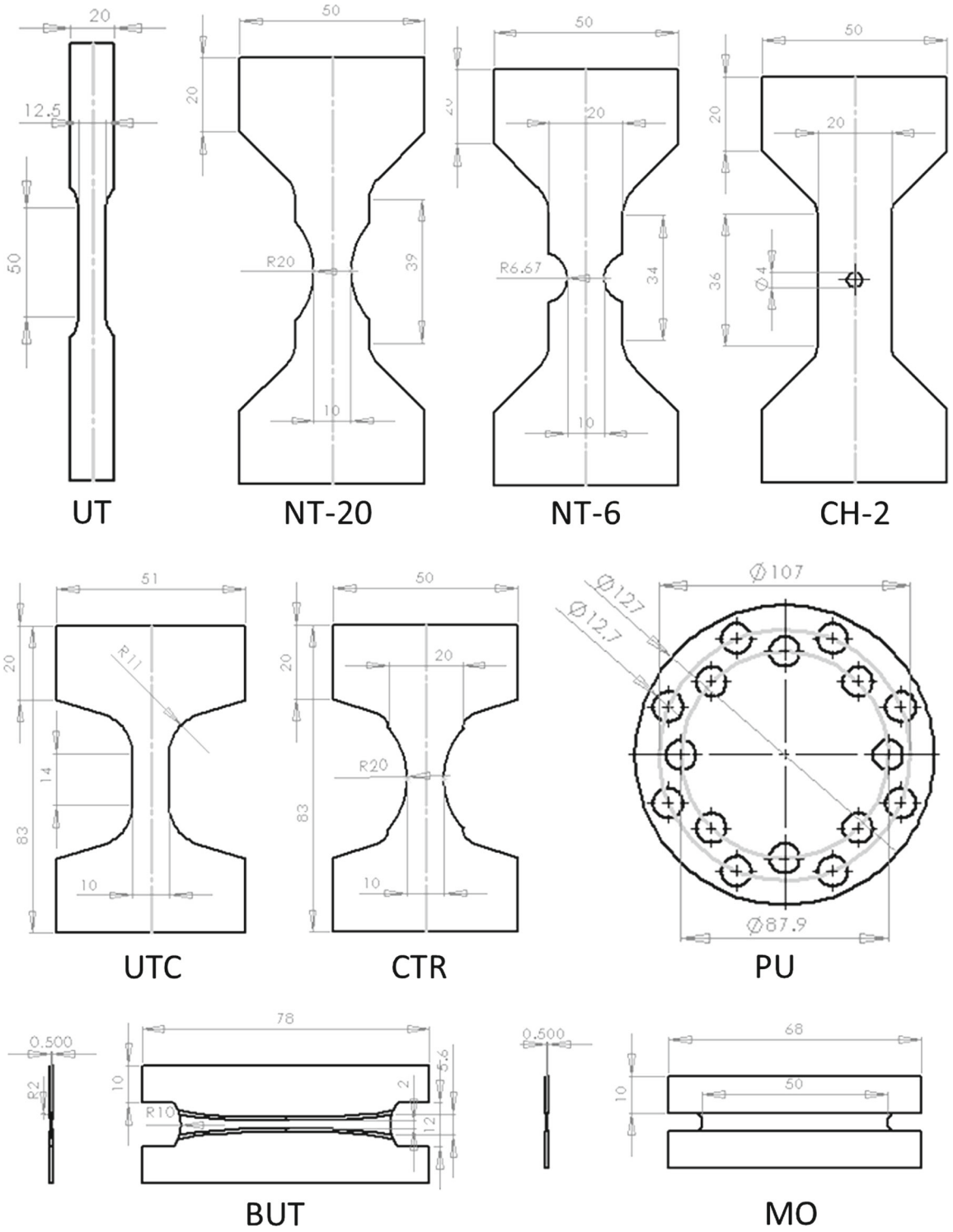

Fig. 5 Drawings of all specimens employed: flat dogbone specimen for uniaxial tension (UT), tension specimens with different notch radii (NT20, NT6), central hole tension specimen (CH2), uniaxial tension–compression specimen (UTC), notched compression–tension specimen (CTR), punch specimen (PU), butterfly fracture specimen (BUT), and Mohr–Owald specimen (MO)

are positioned into a universal testing machine and loaded at a constant cross-head velocity of 2 mm/min. In addition to the axial strain, the width strain is measured using planar Digital Image Correlation (DIC);

(b) Monotonic notched tension (NT): the minimum gage section width of all notched specimens was 10 mm (Fig. 5), while the notch radii were either 20 mm (NT-20) or 6.67 mm (NT-6). The notched specimens were loaded at constant cross-head velocity of 0.5 mm/min all the way to fracture. The relative axial shoulder displacements were measured using 17 and 15 mm long DIC extensometers for the NT-6 and NT-20 specimens, respectively. In addition, a local relative displacement has been measured using a 2 mm long virtual extensometer at the specimen center;

(c) Monotonic central hole tension (CH): the employed tensile specimens were 20 mm wide and featured a 4 mm diameter hole at the gage section center; as for the NT specimens, a global relative displacement has been measured using a 20 mm long axial virtual extensometer;

(d) Monotonic punch experiments (PU): the disc specimen is clamped onto a 100 mm diameter die and subjected to out-of-plane loading using a 44.5 mm diameter hemispherical punch (Dunand and Mohr 2010); the specimen is loaded all the way to fracture at a punch velocity of 5 mm/min. The surface strains are measured in the apex region of the punched specimen using stereo DIC.

(e) Uniaxial tension–compression experiments (UTC): the specimens are first loaded up to an axial strain of 0.1 or 0.2 under uniaxial tension, before loading direction reversal. A low friction anti-buckling device is employed to apply compression stain increment of up to 0.15 before buckling failure. The axial strains are monitored in these experiments using a 12 mm long virtual extensometer;

(f) Notched compression–tension experiments (CTR): notched specimens (Fig. 5) with the same gage section dimensions as the NT-20 specimens are first subject to compressive strains of up to -0.13, before removing the anti-buckling device and loading the specimen all the way to fracture under tension; the global and local axial DIC extensometer lengths are 12 and 2 mm, respectively.

(g) Reverse shear plasticity experiments (MO): tangential loading is applied onto a rectangular specimen (Fig. 5), while keeping the vertical force zero (Mohr and Oswald 2008). The strains are measured within the 5 mm high and 50 mm long gage section using planar DIC. To avoid any plastic deformation in the gripping areas and to reduce the required tangential forces, the gage section thickness is reduced to 0.5 mm using conventional milling. Fracture initiates near the gage section edges which limits the validity of the experiments to equivalent strain levels of about 0.3 for monotonic loading; the experiment are performed in a tangential displacement-control mode at a constant velocity of 0.2 mm/min;

(h) Reverse shear fracture experiments (BUT): in close analogy with the shear plasticity experiments, tangential loads are applied to a butterfly-shaped specimen (Fig. 5, Dunand and Mohr 2011). Different from the MO specimen, fracture initiates near the specimen center where the stress state is close to pure shear. The relative tangential and normal displacement of the specimen shoulders is monitored using planar DIC. All experiments are performed a constant tangential velocity of about 0.2 mm/min, while keeping the normal force zero.

4.3 Details on experimental procedures

The experimental procedures for experiment types (a)–(f) have been described in detail in Dunand and Mohr (2010), Mohr and Marcadet (2015) and Marcadet and Mohr (2015). We therefore limit our detailed description to the experimental procedures for the reverse shear experiments which have not been reported previously.

All shear tests are performed on a custom-made Instron dual actuator system (Fig. 6). The boundary conditions and the alignment are well controlled by the high pressure grips. The vertical actuator controls the vertical load applied to the top of the specimen. The horizontal actuator is under displacement control.

4.3.1 Reverse shear plasticity experiments

The high width to height ratio of the MO specimen ensures that the shear stress field is approximately uniform within the specimen gage section; it can therefore be calculated based on the force measurements at the specimen boundaries. After machining the specimens, a random speckle pattern is applied onto the gage section surface. A digital camera equipped with

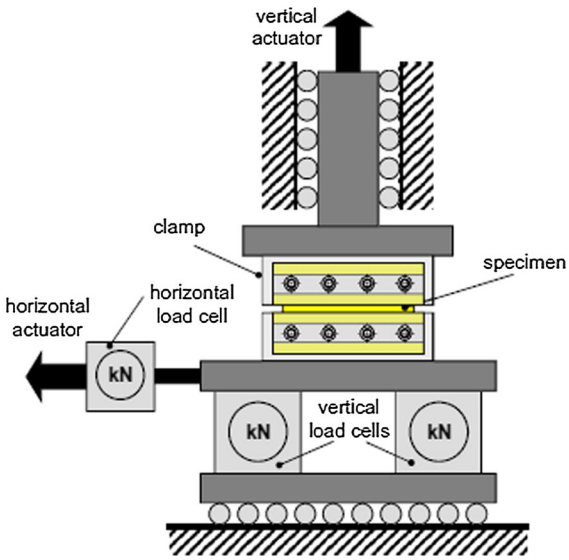

Fig. 6 Dual actuator system

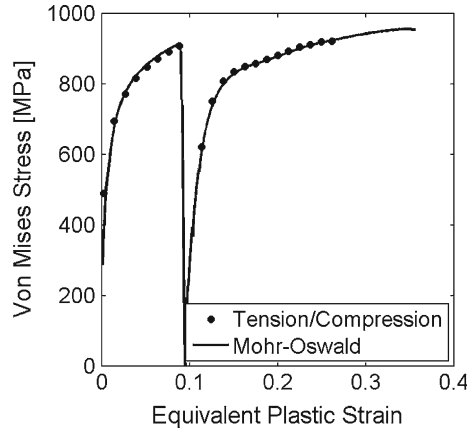

Fig. 7 Comparison of the stress–strain response of DP780 steel in an experiment with loading reversal at an equivalent plastic strain of 0.1. The *solid curve* has been determined from a Mohr–Oswald shear experiment, while the *dotted curve* has been obtained from a uniaxial experiment with tension followed by compression

Nikon 105 mm 1:1 macro lenses monitored the central part of the gage section at a frame rate of 1 Hz. The tangential displacement is applied at a constant horizontal actuator speed of 0.5 mm/min. The experiments are aborted as soon as small cracks become visible by eye in the gage section corners. The reader is referred to Mohr and Oswald (2008) for details on the stress–strain curve extraction. An example equivalent stress versus equivalent plastic strain curve for the DP780 material for an MO experiment with loading reversal at a strain of about 0.09 is shown in Fig. 7. In the same figure, we also show the stress–strain curve from a tension–compression experiment (UTC specimen) with loading reversal at the same equivalent plastic strain (solid dots). The remarkable agreement of both curves is seen as a partial validation of the reverse loading testing techniques. Furthermore, it illustrates that significantly larger strains could be achieved with the MO specimen (before the formation of corner cracks) than in a UTC specimen (which fails due to buckling).

4.3.2 Reverse shear fracture experiments

As mentioned above, the MO specimen fails because of strain concentrations at the gage section corners and is thus not suitable for measuring the strain to fracture for pure shear. Instead, the butterfly (BUT) specimen (Fig. 5) introduced by Dunand and Mohr (2011) is used. It features slightly curved specimen shoulders which generate significantly larger strains at the specimen center than at the free gage section boundaries. As a result, fracture initiates near the gage section center where pure shear conditions prevail.[1]

A velocity of 0.5 mm/min is applied to the horizontal actuator, while keeping the vertical force zero. The horizontal and vertical relative displacements Δu and Δv of the specimen shoulders is measured using an DIC extensometer at an acquisition frequency of 1 Hz. Due to the heterogeneity of the mechanical fields, the equivalent plastic strain evolution at the specimen center is extracted from a finite element simulation of the experiment. Following the modeling guidelines of Dunand and Mohr (2011), we made use of a solid element mesh with four first-order elements along the half-thickness of the specimen gage section (i.e. an element size of about 0.06 mm). The instant of loading reversal in reverse loading experiment is then also determined after computing the strain evolution for a monotonic experiment.

4.4 Overview on experiments performed

The same battery of monotonic experiments has been completed for both materials:

[1] This statement holds true for most engineering materials tested so far. However, it is important to verify the validity of this assumption for each experiment performed.

- Uniaxial tension (UT) for three different loading directions
- Central hole and notched tension (CH, NT20 and NT6) along the rolling direction
- Punch (PU) experiment
- Mohr–Oswald (MO) and butterfly (BUT) shear with the rolling direction parallel to the vertical axis

For the DP590 steel, the effect of loading direction reversal has been characterized using

- Reverse Mohr–Oswald (MO) shear plasticity experiments with loading reversal at an equivalent plastic strain of 0.1 and 0.2;
- Reverse butterfly (BUT) shear fracture experiments with loading reversal at an equivalent plastic strain of 0.25 and 0.50;

For the DP780 steel, a more extensive experimental program has been performed to investigate the effect of loading direction reversal:

- Uniaxial tension–compression (UTC) experiments with loading direction reversal at an equivalent plastic strain of 0.05 and 0.1;
- Notched compression–tension (CTR) experiments with loading direction reversal at an equivalent plastic strain of 0.05, 0.10, 0.15 and 0.20;

We intentionally chose nearly isotropic AHSS sheet materials to defer the investigation of the possible combined effect of initial anisotropy and loading direction reversal to future work. In our fracture testing program, we do not consider different specimen orientations and perform all experiments along the rolling direction only. Consequently, the conclusions drawn from this study will be only be validated experimentally through rolling direction data. The main purpose of the performed experiments is to serve as basis for material model identification and model validation. We omit a separate discussion of the experimental observations per se in the present section. Instead, the experimental results are introduced in the next section on the model application and validation.

From a mechanistic point of view, it is noted that through thickness necking was observed in specimens (a)–(c) and (e)–(f). The final fracture surfaces are slant, i.e. oriented at an angle of about 45° with respect to the sheet thickness direction.

Table 1 Lankford ratios

	r_0 (–)	r_{45} (–)	r_{90} (–)
DP590	0.98	0.84	1.13
DP780	0.78	0.96	0.77

5 Application and validation

The newly-proposed plasticity and fracture models are applied to describe the large deformation response of the DP780 and DP590 dual phase steels. It is emphasized that the material is nearly isotropic in its initial state, i.e. the axial stress–strain response is direction-independent and the Lankford ratios are also only mildly direction dependent (Table 1). The use of an associated (isotropic) flow rule would yield almost the same results for the above materials. The fracture model is fully isotropic for monotonic loading, i.e. the possible effect of initial anisotropy is neglected. However, both the plasticity and fracture models account for the effects of deformation-induced anisotropy which is represented by the evolution of the back stress tensors.

5.1 Plasticity model parameter identification

The proposed plasticity model features the following material parameters:

- anisotropic flow potential parameters $\{G_{12}, G_{22}, G_{44}\}$
- Swift–Voce parameters $\{\varepsilon_0, A, n, Y_0, Q, b_V, w\}$
- kinematic hardening parameters $\{C_\beta, \gamma_\alpha, \gamma_\beta\}$
- hardening stagnation parameter h

As mentioned above, the great advantage of the model over our earlier formulation (Marcadet and Mohr 2015) is that these parameters can be identified sequentially.

5.1.1 Monotonic loading

Firstly, the flow potential parameters $\{G_{12}, G_{22}, G_{44}\}$ are determined from the Lankford coefficients,

$$G_{12} = -\frac{r_0}{1+r_0},$$
$$G_{22} = \frac{r_0}{r_{90}}\frac{1+r_{90}}{1+r_0}, \text{ and}$$
$$G_{44} = \frac{1+2r_{45}}{r_{90}}\frac{r_0+r_{90}}{1+r_0}. \tag{58}$$

Table 2 Swift–Voce model parameters

	Y_0 (MPa)	Q (MPa)	b_V (–)	A (MPa)	ε_0 (–)	n (–)	w (–)
DP590	345.9	335.8	24.9	1031.0	0.0013	0.2	0.73
DP780	614.0	270.0	32.2	1170.0	$3.1\ 10^{-5}$	0.11	0.79

Then, the Swift parameters $\{\varepsilon_0, A, n\}$, and the Voce parameters $\{Y_0, Q, b\}$ are independently determined from a fit to the measured true stress versus plastic strain curve for uniaxial tension along the rolling direction.

Finally, the parameter w is determined through inverse analysis; it is chosen such that the predicted load-displacement response for the NT20 specimen matches the experimental result. During this optimization, the parameters for reverse loading are set to dummy values (e.g. $C_\beta = 0$, $\gamma_\alpha = 100$, $\gamma_\beta = 100$, $h = 0$) since they have a negligible effect on the simulation results. The final set of parameters for monotonic loading is given in Table 2.

5.1.2 Reverse loading

In the proposed plasticity model, the effects of the parameters for reverse loading are nearly independent, and do not affect the response of the model under proportional loading conditions. The dimensionless parameter γ_α controls the rate of transient hardening in the Bauschinger phase. The dimensionless parameter h controls the finite strain increment during which work hardening stagnation takes place. The parameter C_β controls the strength reduction related to permanent softening, while the dimensionless parameter γ_β controls the rate of strain hardening after the end of the work hardening stagnation phase. The effect of each model parameter is illustrated in Fig. 1.

The von Mises stress versus equivalent plastic strain relation is numerically evaluated using a single element simulation. The boundary conditions are such that the element is under simple shear (or uniaxial tension); loading reversal is applied at the corresponding equivalent plastic strain as obtained with the MO experiments (or UTC experiments). The predicted stress–strain response is then compared to the experimental response. The parameters $x = \{C_\beta, \gamma_\alpha, \gamma_\beta, h\}$ are determined such as to minimize the difference between the experimentally-measured and numerically-predicted curves. The error function is expressed as

Table 3 Kinematic hardening and stagnation parameters

	C_β(MPa)	γ_α (–)	γ_β (–)	h (–)
DP590	51.3	74.8	2.1	0.49
DP780	231.6	65.2	6.0	0.64

$$\Gamma_I[x] = \sqrt{\sum_{j=1}^{2}\sum_{m=1}^{M_j}\left(\frac{\sigma_j^{SIM}[\varepsilon_m^{EXP}]}{\sigma_j^{EXP}[\varepsilon_m^{EXP}]} - 1\right)^2} \tag{59}$$

where the subscript $j = 1, 2$ differentiates among the stress–strain curves for different levels of pre-strain; M_j denotes the total of experimental data points used for the computation of the residual for the experiment j.

This inverse identification procedure has been performed using a Nelder–Mead optimization algorithm (Matlab) in conjunction with Abaqus. For the DP590 steel, the MO experiments have been used to identify the parameters $\{C_\beta, \gamma_\alpha, \gamma_\beta, h\}$, while the UTC experiments have been used for the DP780 steel. The final model parameters are listed in Table 3. The corresponding comparison of the numerical (solid red) and experimental (dashed black) curves are shown in Fig. 8a for the DP590 steel, and in Fig. 8b for the DP780 steel. It is reemphasized that the model response for monotonic loading remained approximately unchanged after identifying the kinematic hardening and stagnation parameters, which is seen as a significant simplification of the complex and tedious process of the parameter identification of our previous CCY plasticity model (Marcadet and Mohr 2015).

A validation of the identified plasticity model parameters is given in Figs. 9 and 10 for the DP780 steel, where we simulated the butterfly shear experiments with loading reversal and the notched compression–tension experiments for different levels of pre-strain.

5.2 Fracture model parameter identification

The critical hardening rate model set of parameters $\{a, H_{UT}, c\}$ is identified from the monotonic fracture

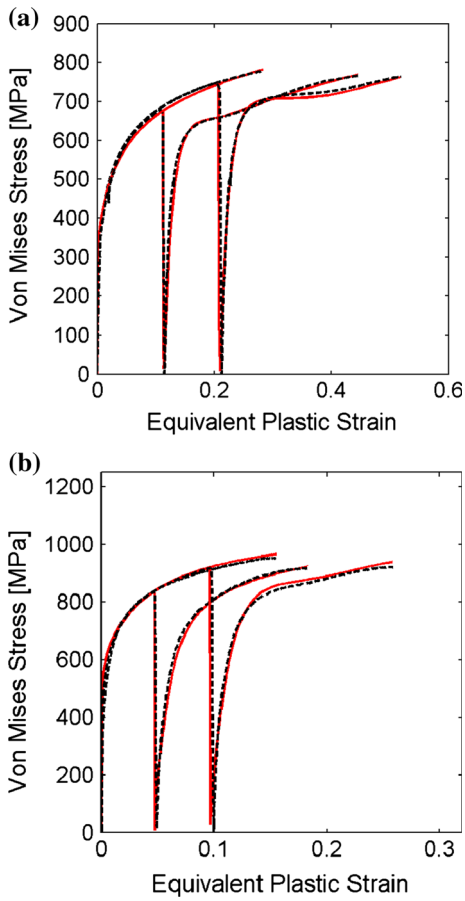

Fig. 8 Comparison of the von Mises stress versus equivalent plastic strain curves after loading reversal for experimental data (*black dotted line*) and the prediction of the model after calibration (*red solid line*) for: **a** reverse shear on a MO specimen extracted from DP590, and **b** tension–compression loading of a DP780 UTC specimen

experiments for five different stress states: NT6, NT20, CH, BUT and PU. In all experiments, the instant of fracture initiation is determined through a sudden force drop. This instant always coincided with the emergence of a clearly visible (by eye) macroscopic crack. From the simulation of each experiment, we extract the loading path to fracture, i.e. the evolution of the equivalent plastic strain, the hardening rate, the stress triaxiality and the Lode angle parameter until the instant of fracture initiation. The loading paths to fracture are shown as solid black lines in the equivalent plastic strain versus stress triaxiality plane in Fig. 11a (DP590 steel) and Fig. 11b (DP780 steel). Even though the experiments are highly repeatable (the measured force-

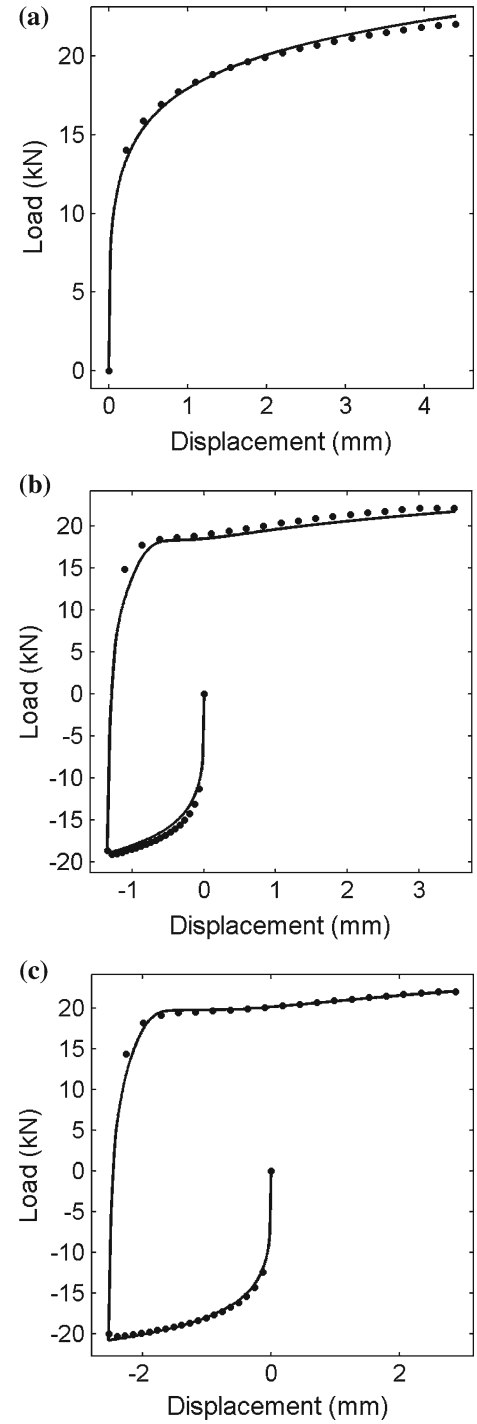

Fig. 9 Comparison of the experimental (*dotted*) and predicted (*solid*) force-displacement curves for experiments on BUT specimens extracted from DP780 steel: **a** monotonic shear, **b** shear reversal at an equivalent plastic strain of 0.25, **c** shear reversal at an equivalent plastic strain of 0.50

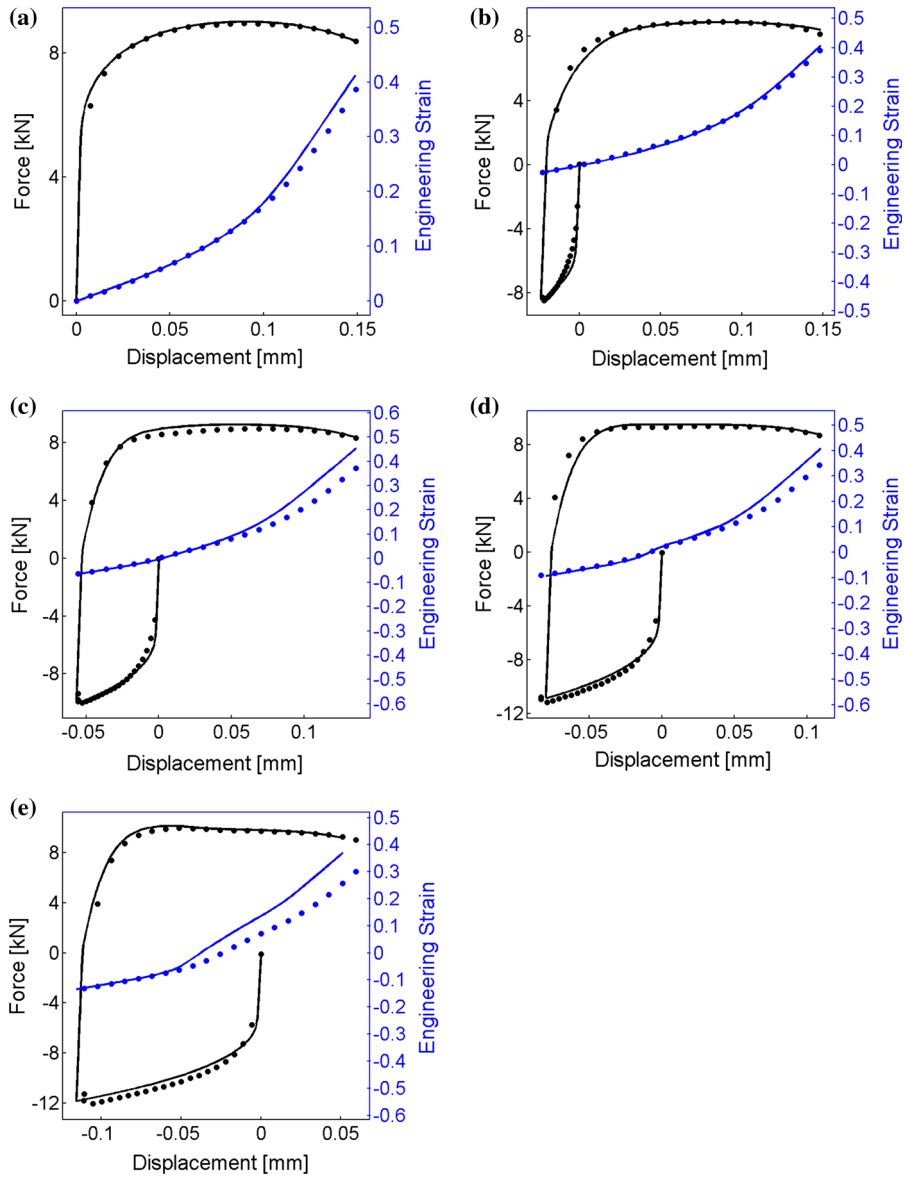

Fig. 10 Comparison of the experimental (*dotted*) and predicted (*solid*) force-displacement curves and local strain evolutions for experiments on CTR specimens extracted from DP780 steel: **a** monotonic tension, and load reversal after compression up to an equivalent plastic strain of **b** 0.05, **c** 0.10, **d** 0.15 and **e** 0.20

displacement curves of repeated experiments lied on top of each other), the computed loading paths to fracture include uncertainties related to the DIC displacement measurement and the plasticity model approximation. The fracture displacement measurement uncertainty of about 10 μm equates to a fracture strain uncertainty of about 0.03. The uncertainty related to the accuracy of the plasticity model is expected to be 0.05 in the reported fracture strains (estimated based on the surface strain comparison shown in Fig. 8). Using a basic Matlab script, the strains to fracture are calculated according to the critical hardening rate model for all given monotonic loading paths, and the parameters $\{a, H_{UT}, c\}$ are identified numerically through residual minimization (taking all five experiments into account). The corresponding instants of fracture initiation as predicted using the model parameters given in Table 4 are shown as solid black dots in Fig. 11. Note that the three-parameter model provides a good fit (less than 3 % error) for all five calibration experiments.

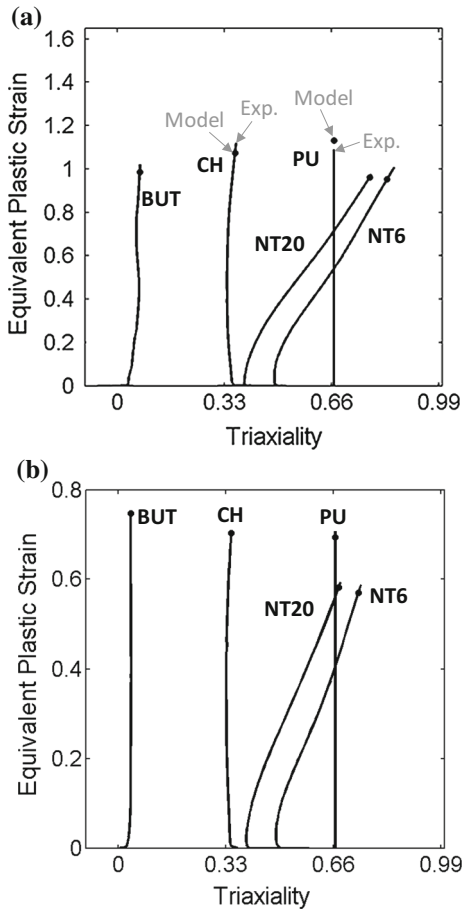

Fig. 11 Calibration of the critical hardening rate model using the results from monotonic experiments on **a** DP590 steel, and **b** DP780 steel. The *ends of the solid lines* correspond to the instant of fracture initiation in the experiments, while the *solid dots* are the model predictions after calibration

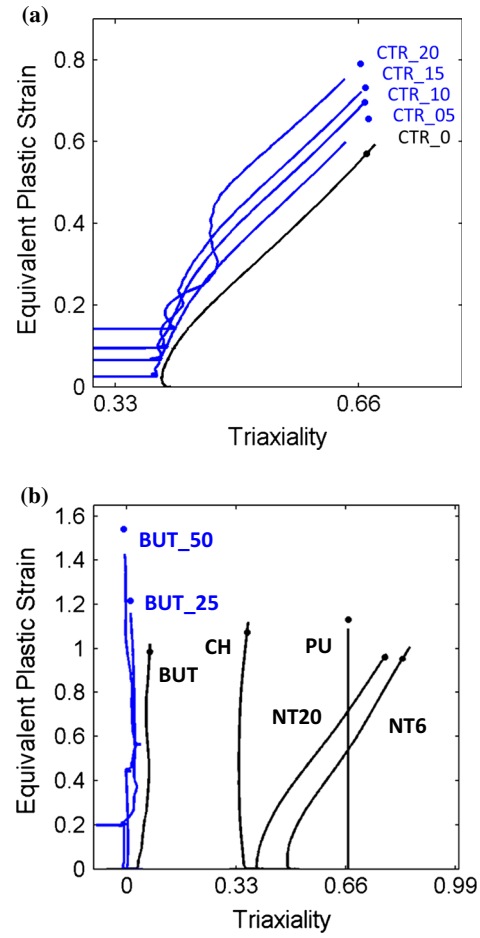

Fig. 12 Model validation for reverse loading experiments: **a** compression followed by tension experiments on DP780 **b** shear reversal experiments on DP590. The *ends of the solid lines* correspond to the instant of fracture initiation in the experiments, while the *solid dots* are the model predictions. Note that none of the *blue curves* has been used for model calibration. Also note that the compression part of the loading path before load reversal is not shown in **a**

Table 4 Critical hardening model parameters

	H_{UT} (MPa)	a (–)	c (–)
DP590	146.3	1.89	0.005
DP780	143.1	1.77	0.022

5.3 Critical hardening rate model validation

The predictive capabilities of the critical hardening rate model are evaluated using the experimental data for fracture initiation after reverse loading (Fig. 12).

For the DP780 steel (Fig. 12a), the computed loading paths for the compression–tension experiments (CTR) are shown as solid blue lines; the end of each curve corresponds to the instant in the simulation, where fracture initiated in the experiment. The instants of fracture initiation predicted by the critical hardening model are highlighted by the solid dots. Note that the predicted strains to fracture coincide with those obtained experimentally for two levels of pre-strain (CTR-10, CTR-15). We reemphasize that the blue dots are true predictions and that no additional parameter was introduced in the fracture model to account for the effect of loading reversal.

For the DP590 steel, the model performance is evaluated for butterfly shear experiments with loading direction reversal at an equivalent plastic strain of 0.25 and 0.50 (Fig. 12b). As for the DP780 steel, we observe

good agreement of the predicted fracture strains (solid dots) and the end points of the loading paths to fracture. Overall, the error in the fracture strain predictions of the critical hardening rate model is less than 8 % for all validation experiments. Note that the critical hardening rate model clearly captures the pronounced increase in ductility due to the shearing direction reversal, which is seen as a major improvement over state of the art damage indicator models.

The general trend is that loading direction reversal increases the strain to fracture. This is due to the increase in hardening rate associated with the transient behavior after loading direction reversal. As far as the stress state sensitivity is concerned, we do not expect any qualitative change related to loading direction reversal, i.e. the same qualitative features of the fracture strain versus stress triaxiality plot shown in Fig. 3c will also be found after loading direction reversal.

6 Conclusions

It is assumed that the onset of ductile fracture in a polycrystalline material is imminent with the formation of a localization band. As a phenomenological alternative to Rice's (1976) localization analysis, it is proposed that localization (and hence ductile fracture) occurs when the effective hardening rate reaches a critical value that is a function of the stress triaxiality and the Lode parameter. According to this approach, the path dependency of ductile fracture is only due to plasticity. To provide an accurate description of the finite strain plasticity of DP steels, a new phenomenological plasticity model is proposed which accounts for the Bauschinger effect, hardening stagnation, permanent softening and non-associated anisotropic plastic flow. The plasticity model is formulated such that its response to monotonic loading remains unaffected when changing the kinematic hardening parameters.

All three parameters of the Hosford–Coulomb based critical hardening rate model are identified from basic monotonic fracture experiments on DP590 and DP780 steel for different stress states (notched tension, central hole tension, punch, butterfly shear). Subsequently, the effect of loading direction reversal at finite strains on the fracture initiation in advanced high strength steels is characterized experimentally through notched compression–tension experiments and reversed butterfly shear experiments. It is shown that the critical hardening rate model provides reasonable predictions of the strain to fracture for all experiments with loading direction reversal. Different from damage indicator models (e.g. Bai and Wierzbicki 2010; Mohr and Marcadet 2015), the new modeling approach can predict the significant increase in ductility due to reverse shearing.

Acknowledgments The partial financial support of MIT Industrial Fracture Consortium is gratefully acknowledged. Special thanks are due to Prof. Tomasz Wierzbicki (MIT) and Dr. Tom Stoughton (GM) for valuable discussions.

References

Anand L, Su C (2005) A theory for amorphous viscoplastic materials undergoing finite deformations, with application to metallic glasses. J Mech Phys Solids 53:1362–1396

Armstrong PJ, Frederick CO (1966) A mathematical representation of the multiaxial bauschinger effect. G.E.G.B, Report RD/B/N 731

Bai Y (2008) Effect of loading history on necking fracture fracture. PhD Thesis. Massachusetts Institute of Technology, Department of Mechanical Engineering, Cambridge USA

Bai Y, Wierzbicki T (2010) Application of the extended Coulomb–Mohr model to ductile fracture. Int J Fract 161:1–20

Bao Y, Wierzbicki T (2004) On fracture locus in the equivalent strain and stresstriaxiality space. Int J Mech Sci 46(1):81–98

Barlat F, Gracio JJ, Lee MG, Rauch EF, Vincze G (2011) An alternative to kinematic hardening in classical plasticity. Int J Plast 27:1309–1327

Barsoum I, Faleskog J (2007) Rupture mechanisms in combined tension and shear—experiments. Int J Solids Struct 44(6):1768–1786

Benallal A, Berstad T, Børvikb T, Clausenb AH, Hopperstad OS (2006) Dynamic strain aging and related instabilities: experimental, theoretical and numerical aspects. Eur J Mech A Solids 25:397–424

Benzerga AA (2002) Micromechanics of coalescence in ductile fracture. J Mech Phys Solids 50:1331–1362

Benzerga AA, Besson J (2001) Plastic potentials for anisotropic porous solids. Eur J Mech 20A:397–434

Benzerga AA, Leblond JB (2010) Ductile fracture by void growth to coalescence. Adv Appl Mech 44:169–305

Besson J, Steglich D, Brocks W (2003) Modeling of plane strain ductile rupture. Int J Plast 19(10):1517–1541

Brozzo P, Deluca B, Rendina R (1972) A new method for the prediction of formability in metal sheets, sheet material forming and formability. In: Proceedings of the 7th biennial conference of the IDDRG

Chaboche JL (2008) A review of some plasticity and viscoplasticity constitutive theories. Int J Plast 24(10):1642–1693

Clift SE, Hartley P, Sturgess CEN, Rowe GW (1990) Fracture prediction in plastic deformation processes. Int J Mech Sci 32:1–17

Cockcroft MG, Latham DJ (1968) Ductility and the workability of metals. J Inst Met 96:33–39

Cvitanic V, Vlak F, Lozina Z (2008) A finite element formulation based on non-associated plasticity for sheet metal forming. Int J Plast 24:646–687

Dafalias Y, Popov E (1976), Plastic internal variables formalism of cyclic plasticity. J Appl Mech 43(41):645–651
Danas K, Ponte Castañeda P (2012) Influence of the Lode parameter and the stress triaxiality on the failure of elasto-plastic porous materials. Int J Solids Struct. doi:10.1016/j.ijsolstr.2012.02.006
Dunand M, Mohr D (2010) Hybrid experimental-numerical analysis of basic ductile fracture experiments for sheet metals. Int J Solids Struct 47(9):1130–1143
Dunand M, Mohr D (2011) Optimized butterfly specimen for the fracture testing of sheet materials under combined normal and shear loading. Eng Fract Mech 78(17):2919–2934
Eggertsen PA, Mattiasson K (2010) On constitutive modeling for springback analysis. Int J Mech Sci 52(6):804–818
Eggertsen PA, Mattiasson K (2011) On the identification of kinematic hardening material parameters for accurate springback predictions. Int J Mater Form 4(2):103–120
Ghahremaninezhad A, Ravi-Chandar K (2012) Ductile failure behavior of polycrystalline Al 6061-T6. Int J Fract 174(2):177–202
Ghahremaninezhad A, Ravi-Chandar K (2013) Ductile failure behavior of polycrystalline Al 6061-T6 under shear dominant loading. Int J Fract 180:23–39
Gologanu M, Leblond J-B, Devaux J (1993) Approximate models for ductile metals containing non-spherical voids—case of axisymmetric prolate ellipsoidal cavities. J Mech Phys Solids 41(11):1723–1754
Gu G, Mohr D (2015) Anisotropic Hosford-Coulomb fracture initiation model: theory and application. Eng Fract Mech 147:480–497
Gurson AL (1977) Continuum theory of ductile rupture by void nucleation and growth: part I-yield criteria and flow rules for porous ductile media. J Eng Mater Technol 99:2–15
Gurtin ME, Fried E, Anand L (2013) The mechanics and thermodynamics of continua. Cambridge University Press, Cambridge
Hall EO (1970) Yield point phenomena in metals and alloys. Plenum Press, New York
Haltom SS, Kyriakides S, Ravi-Chandar K (2013) Ductile failure under combined shear and tension. Int J Solids Struct 50:1507–1522
Hosford WF (1972) A generalized isotropic yield criterion. J Appl Mech 39:607
Kyriakides S (2001) Propagating instabilities in materials. In: Materials science for the 21th century, society of materials science, vol 1, Japan, pp 316–325
LeRoy G, Embury JD, Edward G, Ashby MF (1981) A model of ductile fracture based on the nucleation and growth of voids. Acta Metall 29:1509–1522
Marcadet SJ, Mohr D (2015). Effect of compression–tension loading reversal on the strain to fracture of dual phase steel sheets. Int J Plast 72:21–43
McClintock FA (1968) A criterion of ductile fracture by growth of holes. J Appl Mech 35:363–371
Mear ME, Hutchinson JW (1985) Influence of yield surface curvature on flow localization in dilatant plasticity. Mech Mater 4:395–407
Mohr D, Henn S (2007) Calibration of stress-triaxiality dependent crack formation criteria: a new hybrid experimental-numerical method. Exp Mech 47(6):805–820
Mohr D, Marcadet SJ (2015). Micromechanically-motivated phenomenological Hosford–Coulomb model for predicting ductile fracture initiation at low stress triaxialites. Int J Solids Struct 67–68:40–55
Mohr D, Oswald M (2008) A new experimental technique for the multi-axial testing of advanced high strength steel sheets. Exp Mech 48(1):65–77
Mohr D, Dunand M, Kim KH (2010) Evaluation of associated and non-associated quadratic plasticity models for advanced high strength steel sheets under multi-axial loading. Int J Plast 26(7):939–956
Monchiet V, Cazacu o, Charkaluk E, Kondo D (2008) Macroscopic yield criteria for plastic anisotropic materials containing spheroidal voids. Int J Plast 24:1158–1189
Morgeneyer TF, Taillandier-Thomas T, Helfen L, Baumbach T, Sinclair I, Roux S, Hild F (2014) In situ 3-D observation of early strain localization during failure of thin Al alloy (2198) sheet. Acta Mater 69:78–91
Nahshon K, Hutchinson JW (2008) Modification of the Gurson model for shear failure. Eur J Mech A/Solids 27:1–17
Needleman A, Tvergaard V (1987) An analysis of ductile rupture modes at a crack tip. J Mech Phys Solids 35(1987):151
Oh S, Chen C, Kobayashi S (1979) Ductile failure in axisymmetric extrusion and drawing, part 2, workability in extrusion and drawing. J Eng Ind 101:36–44
Papasidero J, Doquet V, Mohr D (2015) Ductile fracture of aluminum 2024-T351 under proportional and non-proportional multi-axial loading: Bao–Wierzbicki results revisited. Int J Solids Struct 69–70:459–474
Pardoen T, Hutchinson JW (2000) An extended model for void growth and coalescence. J Mech Phys Solids 48:2467–2512
Prager W (1956) A new method of analyzing stresses and strains in work hardening. Plast Solids J Appl Mech ASME 23:493
Rice JR (1976) The localization of plastic deformation. In: Koiter WT (ed) Proceedings of the 14th international congress on theoretical and applied mechanics, vol 1. Delft, pp 207–220
Rice JR, Tracey DM (1969) On the ductile enlargement of voids in triaxial stress fields. J Mech Phys Solids 17:201–221
Stoughton TB (2002) A non-associated flow rule for sheet metal forming. Int J Plast 18(5–6):687–714
Stoughton TB, Yoon JW (2011) A new approach for failure criterion for sheet metals. Int J Plast 27(3):440–459
Sung JH, Kim JN, Wagoner RH (2010) A plastic constitutive equation incorporating strain, strain-rate, and temperature. Int J Plast 26(12):1746–1771
Tardif N, Kyriakides S (2012) Determination of anisotropy and material hardening for aluminum sheet metal. Int J Solids Struct 49:3496–3506
Tekoglu C, Hutchinson JW, Pardoen T (2015) On localization and void coalescence as a precursor to ductile fracture. Philos Trans R Soc A373(2038). doi:10.1098/rsta.2014.0121
Thomason PF (1985) A three-dimensional model for ductile fracture by the growth and coalescence of microvoids. Acta Metall 33:1087–1095
Tvergaard V, Needleman A (1984) Analysis of the cup-cone fracture in a round tensile bar. Acta Metall 32:157–169
Yoshida F, Uemori T (2002) A model of large-strain cyclic plasticity describing the Bauschinger effect and work hardening stagnation. Int J Plast 18(5):661–686